PHOTONICS Research

Dichroic laser mirrors with mixture layers and sandwich-like-structure interfaces

Tingting Zeng,[1,2] Meiping Zhu,[1,2,3,*] Yingjie Chai,[4] Jingping Li,[1] and Jianda Shao[1,2,3,5,6]

[1]Laboratory of Thin Film Optics, Key Laboratory of Materials for High Power Laser, Shanghai Institute of Optics and Fine Mechanics, Chinese Academy of Sciences, Shanghai 201800, China
[2]Center of Materials Science and Optoelectronics Engineering, University of Chinese Academy of Sciences, Beijing 100049, China
[3]Hangzhou Institute for Advanced Study, University of Chinese Academy of Sciences, Hangzhou 310024, China
[4]CREOL, The College of Optics and Photonics, University of Central Florida, Orlando, Florida 32816, USA
[5]CAS Center for Excellence in Ultra-intense Laser Science, Shanghai 201800, China
[6]e-mail: jdshao@siom.ac.cn
*Corresponding author: bree@siom.ac.cn

Received 15 October 2020; revised 29 November 2020; accepted 11 December 2020; posted 15 December 2020 (Doc. ID 411372); published 27 January 2021

The requirements for dichroic laser mirrors continue to increase with the development of laser technology. The challenge of a dichroic laser mirror coating is to simultaneously obtain spectral performance with significantly different reflection or transmission properties as well as a high laser-induced damage threshold (LIDT) at two different wavelengths. Traditional dichroic laser mirrors composed of alternating high- and low-refractive-index pure materials often has difficulty achieving excellent spectral performance and high LIDTs at two wavelengths simultaneously. We propose to use a new design with mixture layers and sandwich-like-structure interfaces to meet the challenging requirements. An Al_2O_3–HfO_2 mixture-based dichroic laser mirror, which can be used as a harmonic separator in a fusion-class laser or a pump/signal beam separator in a petawatt-class Ti-sapphire laser system, is experimentally demonstrated using e-beam deposition. The mixture-based dichroic mirror coating shows good spectral performance, fine mechanical property, low absorption, and high LIDT. For the *s*-polarized 7.7 ns pulses at a wavelength of 532 nm and the *p*-polarized 12 ns pulses at a wavelength of 1064 nm, the LIDTs are almost doubled. The excellent performance of this new design strategy with mixture layers and sandwich-like-structure interfaces suggests its wide applicability in high-performance laser coating.

https://doi.org/10.1364/PRJ.411372

1. INTRODUCTION

Dichroic laser mirrors are usually used as harmonic separators [1,2], beam combiners [3], or beam splitters [4] and play an important role in many laser applications, including inertial confinement fusion (ICF) lasers [5], petawatt femtosecond lasers [6], high power fiber lasers [3,7], compact *Q*-switched or mode-locked lasers [8–10], and other emerging lasers [11]. The ideal dichroic laser mirror for high-power lasers requires a significantly different reflection or transmission property and a high laser-induced damage threshold (LIDT) at two different wavelengths of interest. Unfortunately, a traditional dichroic laser mirror (TDLM) composed of alternating high- and low-refractive-index (n) pure materials often has difficulty achieving excellent spectral performance and high LIDTs at two wavelengths simultaneously [4]. Generally, TDLM for UV-NIR laser applications is achieved by alternately e-beam deposited HfO_2 layers and SiO_2 layers [12]. Sometimes, Al_2O_3 is chosen instead of HfO_2 as the high-n material, which shows improved LIDT but requires a relatively large total number of coating layers [13,14]. There is a trade-off between the required optical performance and LIDT because suitable candidate coating materials are limited. In recent years, the library of available coating materials is expanded by co-evaporated or co-sputtered oxide mixtures [15–17]. The mixture materials provide us with adjustable optical gap values and optical constants, show superior properties over pure materials [16,18], and are attractive for many applications [19–21]. In addition to the coating material itself, it is also necessary to consider the interface-related issues of the traditional discrete interface, which is one of the key factors affecting LIDT. The co-evaporated interface with a graded-refractive index shows a significant increase in LIDT compared with the traditional discrete interface [22,23]. Therefore, by appropriately designing mixture materials and optimizing the interface, it is expected to realize an ideal dichroic laser mirror suitable for high-power lasers.

Here, we propose to use mixture materials combined with a novel sandwich-like interface to meet the challenging requirements of dichroic laser mirrors. First, the HfO_2–Al_2O_3

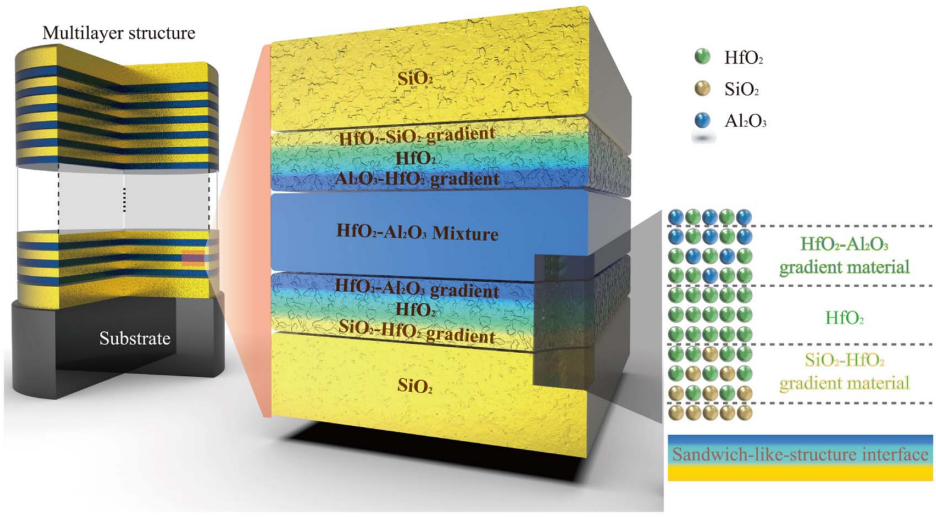

Fig. 1. Schematic diagram of the proposed MDLM design.

mixture coating is compared with pure HfO_2 and Al_2O_3 monolayer coatings as well as HfO_2–Al_2O_3 nanolaminate coatings in terms of microstructure and optical and mechanical properties. Then, a mixture-based dichroic laser mirror (MDLM) is designed and prepared, which uses HfO_2–Al_2O_3 mixture material as a high-n layer with adjustable n and optical bandgap and pure SiO_2 as a low-n material. The schematic diagram of the MDLM design is shown in Fig. 1. The interface between the SiO_2 layer and the HfO_2–Al_2O_3 mixture layer is a sandwich-like-structure interface, which can be represented by "SiO_2–HfO_2 gradient material|HfO_2|HfO_2–Al_2O_3 gradient material." As we will show, this arrangement allows the MDLM design to have excellent spectral performance and high LIDTs at two wavelengths. Our MDLM design strategy, prepared using e-beam evaporation [18], shows improved performance over TDLM and opens new avenues for a variety of laser coatings.

2. MATERIALS AND METHODS

A. Preparation of the Coatings

All coatings are deposited on fused silica and BK7 substrates using e-beam evaporation, in which the HfO_2–Al_2O_3 mixture layer and the sandwich-like-structure interface are obtained by dual e-beam co-evaporation [18]. BK7 and fused silica substrates are used for stress measurement and other measurements, respectively. Before deposition, the coating chamber is heated to 473 K and evacuated to a base pressure of 9×10^{-4} Pa; then, the substrate is cleaned with plasma ions at a bias voltage of 80 V for 120 s. The deposition rates for HfO_2 and Al_2O_3 in monolayer and nanolaminate coatings and the deposition rates for SiO_2 in multilayer coatings are 0.1, 0.1, and 0.2 nm/s, respectively. The deposition rates for HfO_2 and Al_2O_3 in the HfO_2–Al_2O_3 mixture coating are 0.028 and 0.072 nm/s, respectively. The deposition rates for HfO_2 and Al_2O_3 in the mixture layer of the MDLM coating are 0.05 and 0.05 nm/s, respectively. The oxygen pressures of the SiO_2 layer and other layers are 5.0×10^{-3} and 1.3×10^{-2} Pa, respectively.

The schematic diagram of the deposition process of the MDLM coating is shown in Fig. 2. The deposition rate is monitored by a quartz crystal monitor installed at the corresponding side of the coating material. To illustrate the deposition process of the sandwich-like-structure interface, the interface of the HfO_2–Al_2O_3 mixture layer on the SiO_2 layer is taken as an example. First, the deposition rate of the SiO_2 layer is reduced from the set value to 0, and the deposition rate of the HfO_2 layer is increased from 0 to the set value at the same time, thereby forming the SiO_2–HfO_2 gradient material. Then, the deposition rate of the HfO_2 layer is kept constant within the set time. At last, the deposition rate of the Al_2O_3 layer is increased from 0 to the set value, while the deposition rate of the HfO_2 layer remains constant, thereby forming the HfO_2–Al_2O_3 gradient material.

B. Characterization of the Coatings

X-ray diffraction (XRD) (PANalytical Empyrean) is used to characterize the structure information of the coating. A VUV spectrometer (LZH ML 6500) and a UV-VIS-NIR spectrometer (Perkin Elmer Lambda 1050) are employed to measure the transmittance spectra in the ranges of 150–200 nm and 200–1200 nm, respectively. The reflectance spectra in the VIS region are calculated from the transmission data neglecting absorption. The refractive indices and optical bandgaps are estimated using the commercial thin film software (Essential Macleod) and the Tauc equation [24], respectively. The laser-induced temperature rise in the multilayer coating is obtained from the finite-element method (FEM) simulation.

The elemental composition profiles are determined by X-ray photoelectron spectroscopy (XPS, Thermo Scientific K-Alpha) using a monochromatic Al Kα (1486.6 eV) X-ray source. The spectra are recorded after every 20 s of etching with 1 keV Ar^+ ions.

A 632.8 nm wavelength interferometer (ZYGO Mark III-GPI) is employed to inspect the sample surfaces before (substrates) and 60 days after the deposition (coatings) in a controlled environment with a temperature of 23 ± 1.5°C

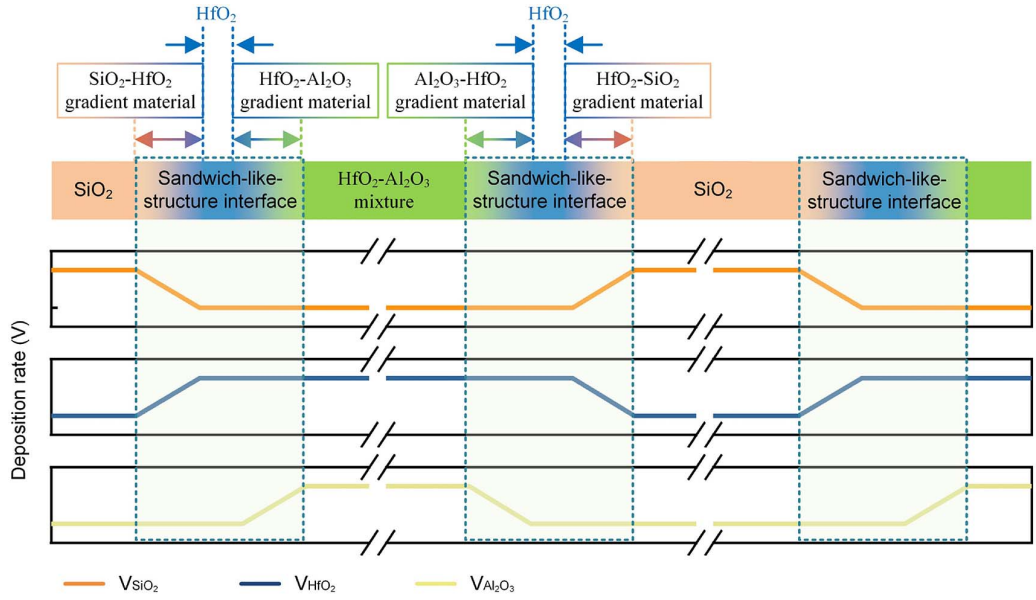

Fig. 2. Schematic diagram of the deposition process of MDLM coating.

and relative humidity of 45% ± 5%. The coating stress is obtained from Stoney's formula.

The absorption of the coating at 1064 nm is measured by a home-made system based on the surface thermal lensing technique. The interfacial adhesion is characterized by a scratch test using a nano indenter (KLA Tencor). A load is gradually increased from 20 μN to 50 mN for the scratch test.

The 1-on-1 LIDT is tested according to ISO 21254. An *s*-polarized 2ω Nd:YAG laser with a 7.7 ns pulse width and a *p*-polarized 1ω Nd:YAG laser with a 12 ns pulse width are used for 532 and 1064 nm LIDT measurements, respectively. The test is performed at an angle of incidence of 45°. The effective beam sizes on the sample surface for 532 and 1064 nm LIDT measurements are approximately 0.32 mm^2 and 0.072 mm^2, respectively. Fifteen sites are tested for each energy fluence. The damage morphology is characterized by a focused ion beam scanning electron microscope (FIB-SEM, Carl Zeiss AURIGA CrossBeam). The chemical composition of the damaged area is analyzed by energy dispersive spectroscopy (EDS, Oxford X-Max, 50 mm^2).

3. EXPERIMENTAL RESULTS AND DISCUSSION

A. Properties of the Pure Monolayer, Nanolaminate, and Mixture Coatings

A HfO_2–Al_2O_3 mixture coating has been prepared and compared with HfO_2 and Al_2O_3 monolayer coatings and HfO_2–Al_2O_3 nanolaminate coatings. The design structures of the nanolaminate coatings are listed in Table 1. The microstructure and optical properties of the coatings have been studied. Multiple sharp diffraction peaks indicating crystallinity are obtained in the XRD pattern of the HfO_2 monolayer coating [Fig. 3(a)]. Two broad peaks at 21.8° and 31.4°, attributed to the amorphous fused silica substrate and HfO_2 (111), are observed in the nanolaminate and mixture coatings. The thinner the HfO_2 sublayer, the less obvious the peak at $2\theta = 31.4°$.

Table 1. Design Information and Extracted Thickness of the Nanolaminate Coatings[a]

Sample Number	Design Structure	Design Thickness in Each B_AB_H Bilayer (nm) B_A	B_H	Total Thickness Fitted by Measured Transmittance (nm)
NL1	Sub|$(B_AB_H)^{10}$|Air	32.5	11.1	427.9
NL2	Sub|$(B_AB_H)^{30}$|Air	11.0	3.9	445.9
NL3	Sub|$(B_AB_H)^{60}$|Air	5.6	2.1	464.9
NL4	Sub|$(B_AB_H)^{60}$|Air	2.9	1.2	259.7

[a]Note: Sub represents the substrate. B_A and B_H represent the Al_2O_3 and HfO_2 layers in the nanolaminate coating, respectively.

To determine *n* and the optical bandgap, the transmittance spectra of the substrate and coating are measured [Fig. 3(b)]. The determined *n* and surface figure change of the mixture and nanolaminate coatings are close [Figs. 3(c) and 3(d)]. The optical bandgap of the nanolaminate coating increases as the thickness of the sublayer decreases, and the mixture layer shows the largest optical bandgap. The dispersion curves of the refractive indices of HfO_2 monolayer, Al_2O_3 monolayer, and HfO_2–Al_2O_3 mixture coatings are derived using the envelope method (Fig. 4). The thicknesses of the HfO_2 monolayer, Al_2O_3 monolayer, and HfO_2–Al_2O_3 mixture coatings are fitted to be 393.3, 513.8, and 433.5 nm, respectively.

The mixture layer has two advantages over the nanolaminate layers: the deposition process is simpler, and the bandgap is larger when *n* is close. The mixture is therefore chosen as the high-*n* material for MDLM coating in this work. This allows one to develop MDLM coatings with excellent optical and LIDT properties.

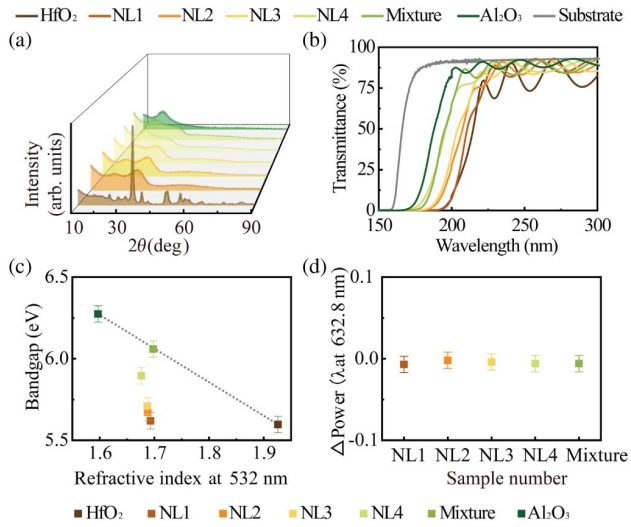

Fig. 3. Microstructure and optical property of the pure monolayer, nanolaminate, and mixture coatings. (a) XRD spectra, (b) transmittance, and (c) optical bandgap versus n of HfO_2 monolayer, Al_2O_3 monolayer, HfO_2–Al_2O_3 nanolaminate, and mixture coatings. (d) Surface figure change (ΔPower) caused by the HfO_2–Al_2O_3 nanolaminate and mixture coatings.

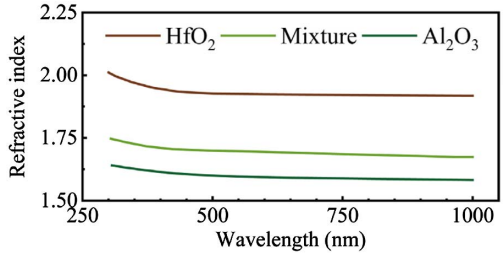

Fig. 4. Dispersion curves of refractive indices of HfO_2 monolayer, Al_2O_3 monolayer, and HfO_2–Al_2O_3 mixture coatings.

B. Mixture-Based Dichroic Laser Mirrors with Sandwich-like-Structure Interfaces

An MDLM coating is designed to achieve an s-polarized reflectivity (Rs) higher than 99.5% at 527 ± 15 nm and a p-polarized transmittance (Tp) higher than 98% in the range of 720 to 1064 nm for an angle of incidence of 45°. This MDLM coating can act as a 1ω and 2ω harmonic separator in fusion-class lasers or a pump/signal beam separator in petawatt-class Ti-sapphire laser systems. The coating structure is as follows: substrate|2L(0.5ML0.5M)^{14}4.45L|air. Here, M and L represent HfO_2–Al_2O_3 mixture and SiO_2 layers with a quarter-wavelength optical thickness (QWOT) at 595 nm (λ_0), respectively. The numbers before M and L represent the optical thickness in units of the QWOT of the corresponding material. The design thickness of the sandwich-like-structure interface is about 12 nm, including SiO_2–HfO_2 gradient material (~4 nm), HfO_2 material (~4 nm), and HfO_2–Al_2O_3 gradient material (~4 nm). The n of L and M at 595 nm are 1.446 and 1.80, respectively. According to $n_M d_M = n_L d_L = \lambda_0/4$, the physical thicknesses are $d_{2L} = 205.74$ nm, $d_{0.5M} = 41.32$ nm, $d_L = 102.87$ nm, and $d_{4.45\,L} = 457.77$ nm. A thick SiO_2 overcoat layer (4.45L) is used as a protective layer, and the resulting electric (E)-field intensity (incident angle at 45°, s-polarized light) of the coating–air interface is close to zero at 532 nm. For comparison, the MDLM coating and a TDLM coating with a substrate |2L(0.5HL0.5H)^{10}4.45L|air structure are prepared. H represents HfO_2 layers with a QWOT at 595 nm, and the physical thickness $d_{0.5H} = 38.66$ nm. The elemental percentage profiles from the high-n layer to the low-n layer in the TDLM and MDLM coatings are compared in Fig. 5.

Obvious sharp diffraction peaks are not observed in the XRD pattern of MDLM but in that of the TDLM coating [Fig. 6(a)]. The MDLM coating shows a lower optical absorption in the short wavelength region. Both coatings show Rs higher than 99.5% at 532 ± 15 nm and Tp higher than 98% in the range of 720 to 1064 nm as designed [Fig. 6(b)]. The surface profiles of the samples before and after coating are compared in Fig. 6(c); the stresses of the TDLM and MDLM coatings are calculated to be −20.1 MPa and −81.2 MPa, respectively. The larger compressive stress of MDLM coating indicates that it can withstand a lower humidity environment than the TDLM coating. The surface and cross-section morphologies after the scratch test [Fig. 6(d)] show that the delamination damage of the MDLM coating is more moderate than that of the TDLM coating, which indicates that the MDLM coating has better mechanical properties. The measured absorption (at 1064 nm) of the MDLM coating is 6 ppm (parts per million), which is half of 12 ppm of the TDLM coating. The laser damage probability as a function of fluence for the two coatings is shown in Fig. 6(e). The damage probability curve under 532 nm laser irradiation is used to extract the defect parameters by using the model developed by Krol *et al.* [25], assuming the existence of two classes of defects with different values of the LIDT T_i and area density D_i (integrated over the thickness) for both coatings. The obtained defect parameters are listed in Table 2, in which the ΔT_i is the threshold standard deviation. More than two typical damage morphologies in one damage site are observed after p-polarized 1064 nm laser irradiation, indicating a more complex damage mechanism, which makes the defect-parameter-extract model difficult to apply. Overall, the LIDT (the maximum laser fluence corresponding to the damage probability of 0%) of the MDLM coating is almost twice that of TDLM coating at both wavelengths.

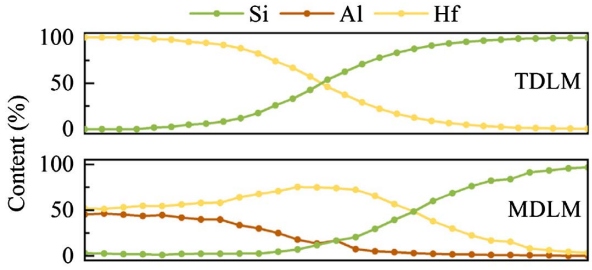

Fig. 5. Elemental percentage profiles from the high-n layer to the low-n layer.

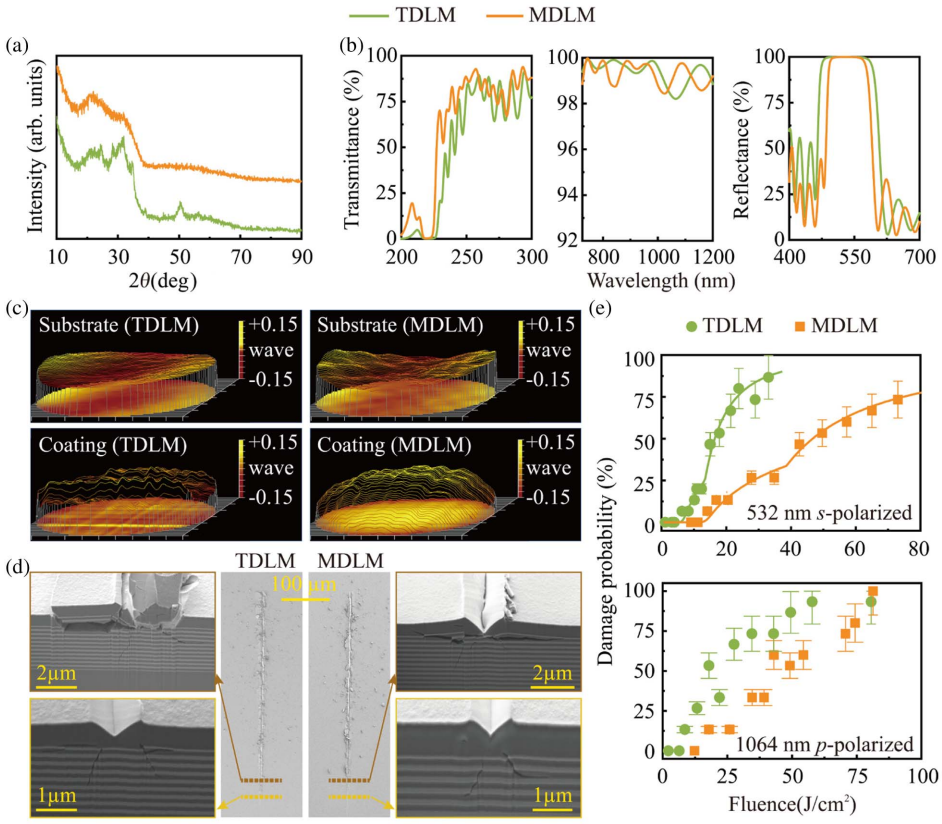

Fig. 6. Microstructure and optical property of the TDLM and MDLM coatings. (a) XRD spectra. (b) Transmittance (left: incident angle at 0°; middle: incident angle at 45°, *p*-polarized light) and reflectance spectra (right: incident angle at 45°, *s*-polarized light). (c) Surface figures of the samples before and after coating. (d) Surface and cross-section morphologies after the scratch test. (e) Single-pulse damage probability as a function of the input fluence.

Table 2. Extracted Defect Parameters

	D_1 (mm^{-2})	T_1 (J/cm^2)	ΔT_1 (J/cm^2)	D_2 (mm^{-2})	T_2 (J/cm^2)	ΔT_2 (J/cm^2)
TDLM	3.5	6.8	1.5	18.5	12.6	1.0
MDLM	3.3	13.7	2.0	12.3	29.2	1.0

Typical damage morphologies of the TDLM and MDLM coatings irradiated by an *s*-polarized 532 nm laser [Figs. 7(a)–7(d)] suggest that both coatings have two different morphological features. The two morphological features in the TDLM coating are shell-type pits [Fig. 7(e)] and flat bottom pits [Fig. 7(f)] observed at laser fluence just above the LIDT and the higher laser fluences, respectively. The two morphological features in the MDLM coating are flat bottom pits [Fig. 7(g)] and nodular-ejected pits [Fig. 7(h)] observed at laser fluence just above the LIDT and the higher laser fluences, respectively. Plasma scalds surrounding the flat bottom pits and nodular-ejected pits are observed at a relatively high laser fluence [Figs. 7(i) and 7(j)]. In general, the shell-type pits are smaller and shallower than the flat bottom pits, and the size of the shell-type and flat bottom pits does not strongly depend on the laser fluence. A nanoscale pinpoint is observed inside the most damaged sites, which indicates that the damage morphology is related to nanoscale defects.

More morphological features are observed after *p*-polarized 1064 nm laser irradiation [Figs. 8(a)–8(i)] because the defect distribution depends on the polarization and wavelength of the study [26]. As shown in Figs. 8(a) and 8(b), multiple pits are observed in the damaged area induced by a single laser shot. At higher laser fluence, plasma scalds are also observed. The typical morphologies are further classified according to their features. In addition to flat bottom pits [Fig. 8(j)] and nodular-ejected pits [Fig. 8(k)] similar to those observed after *s*-polarized 532 nm laser irradiation, two other morphological features observed may be related to substrate defects [27–29], namely, craters [Fig. 8(l)] and pits with microcracks [Fig. 8(m)]. The craters are similar to those observed in fused silica [30]. The microcrack damage may be related to the extensive fractures in the subsurface layer of fused silica. Fracture-induced absorption [27] may cause local temperature rise under laser irradiation and induce damage. The energy dispersive spectroscopy characterization confirms the presence of coating material in the microcracks (Fig. 9), which indicates that local high temperatures are generated under laser irradiation, causing the coating material to melt and enter the cracks. Based on the observed typical damage morphologies, damage may be initiated at three locations: the seeds of the nodules [Figs. 7(d), 8(d), and 8(h)],

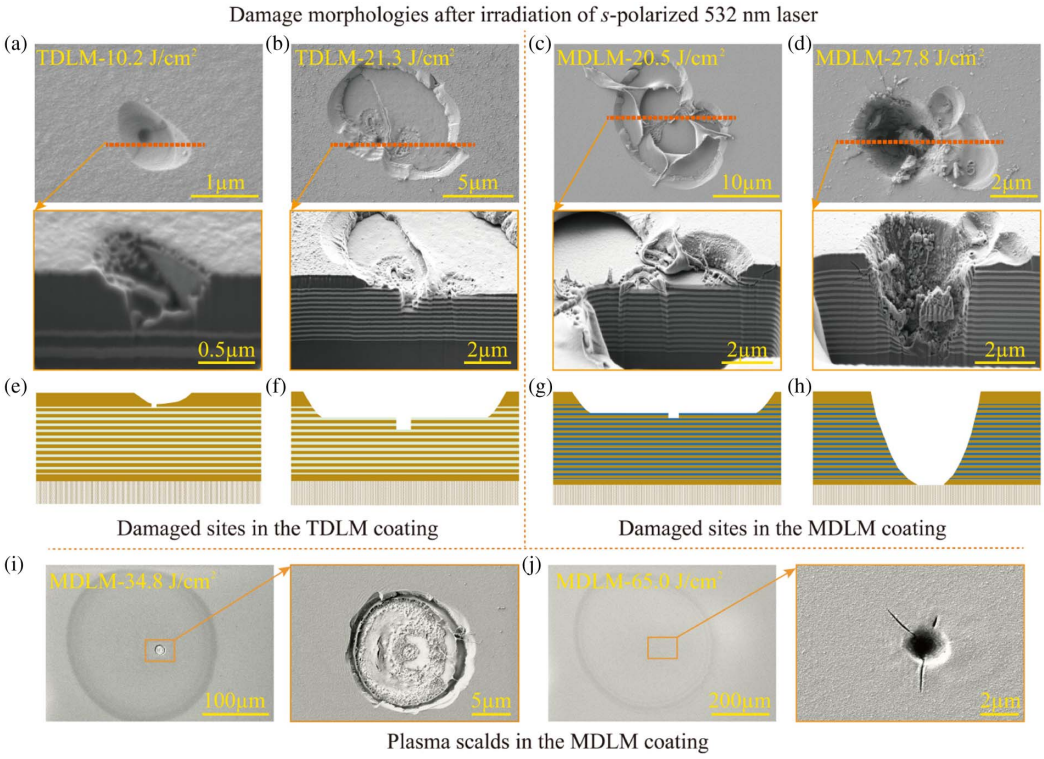

Fig. 7. Damage morphology imaged by SEM and the depth profile of the marked area measured by FIB. (a)–(d) Damaged sites and (e)–(h) schematic diagram of the damage morphologies after irradiation of an *s*-polarized 532 nm laser. (i) and (j) Plasma scald induced by *s*-polarized 532 nm laser in MDLM coating.

nano-precursors at the interface of the SiO_2 layer on the high-n layer [Figs. 7(a)–7(c), 8(c), and 8(g)], and substrate defects especially for the *p*-polarized 1064 nm laser [Figs. 8(e), 8(f), and 8(i)].

An FEM simulation is used to investigate the 1064 nm *p*-polarized laser-induced temperature rise in the two coatings. The extinction coefficients (k) of the HfO_2 layer (1.36×10^{-6}) and HfO_2–Al_2O_3 mixture layer (4.52×10^{-7}) are calculated by using Eq. (1) [31], based on the measured absorption, neglecting the absorption of the SiO_2 layers:

$$1 + \frac{A}{T} = \exp(4\pi kd/\lambda), \tag{1}$$

where A and T are the absorption and the transmittance of coating, d is the coating thickness (only the layers with absorption are taken into account), and λ is the wavelength. The extinction coefficient of dielectric materials typically increases with the decrease of wavelength; in this work, the mixture layer suggests a lower extinction coefficient over the whole wavelength range of interest than the HfO_2 layer.

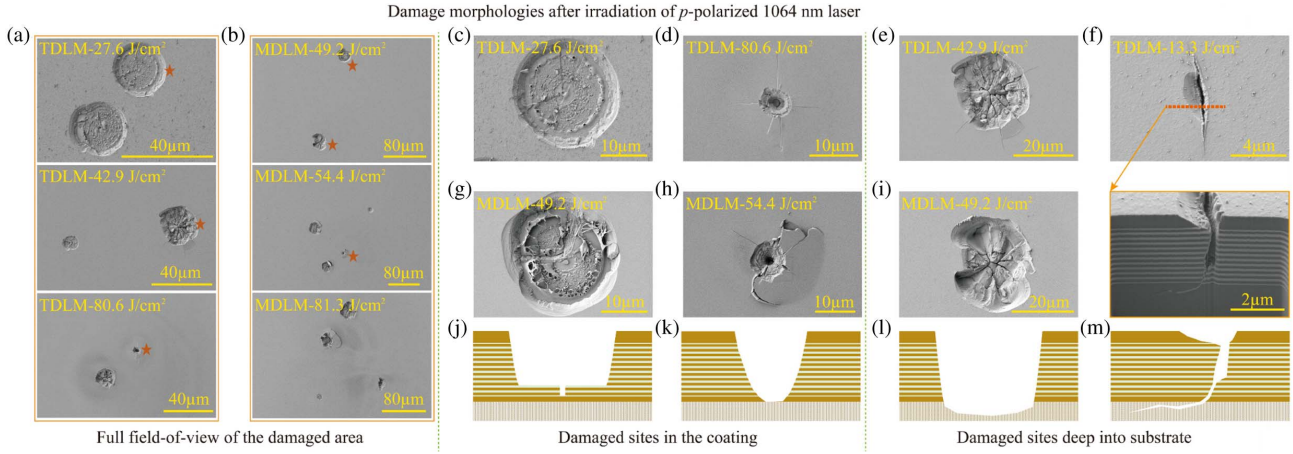

Fig. 8. Damage morphology imaged by SEM and the depth profile of the marked area measured by FIB. (a) and (b) Full field-of-view of the damaged area. (c)–(i) Typical damaged sites marked with asterisks. (j)–(m) Schematic diagram of the damage morphologies after irradiation of a *p*-polarized 1064 nm laser.

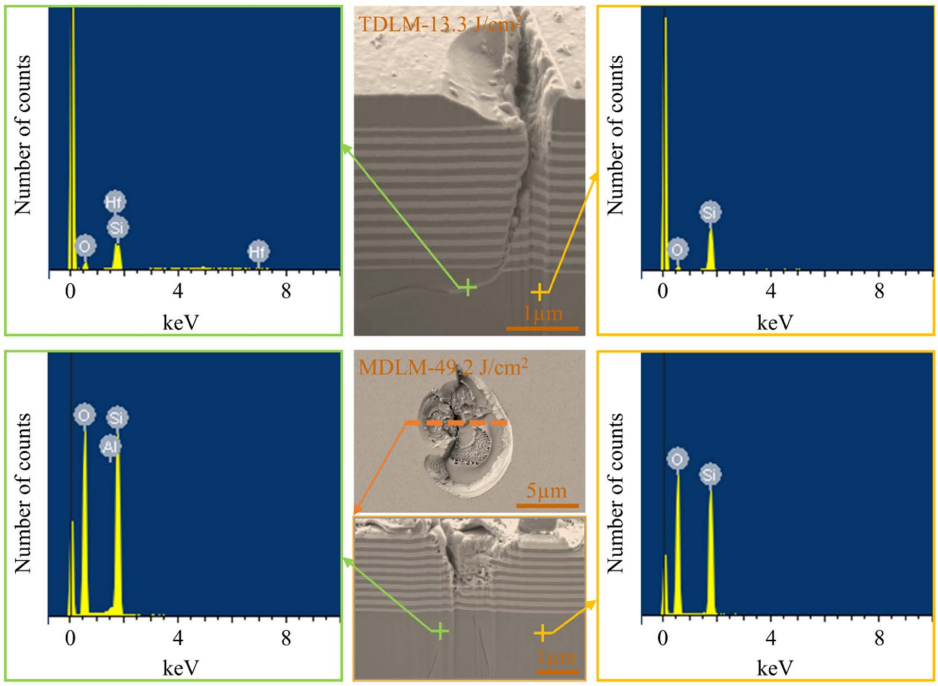

Fig. 9. EDS characterized chemical composition of the damaged site of the TDLM coating and MDLM coating induced by 1064 nm *p*-polarized laser.

For comparison, the input laser parameters for the TDLM coating and MDLM coating are consistent. Figure 10 shows the simulated temperature distributions in the event that a maximum temperature of 1600°C is generated in the TDLM coating, and the simulated temperature rise distributions in the MDLM coating under the same laser input parameters. The maximum temperature in the TDLM coating is almost twice of that of the MDLM coating. Compared with the TDLM coating, the MDLM coating shows a lower laser-induced temperature rise due to its smaller absorption, which is consistent with the higher LIDT observed.

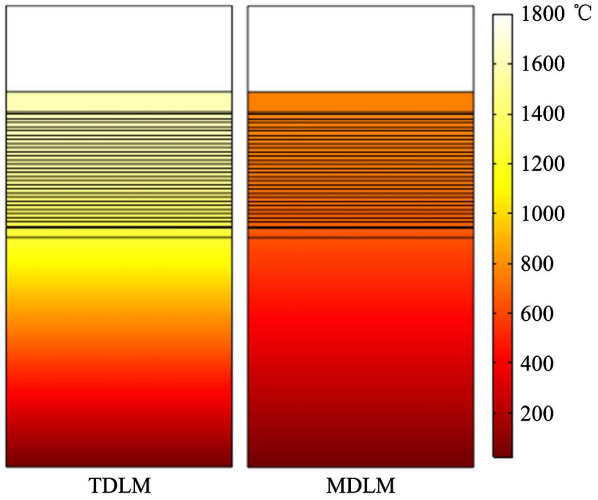

Fig. 10. Simulated laser-induced temperature rises in TDLM and MDLM coatings.

4. SUMMARY

In summary, we have proposed and experimentally demonstrated a new MDLM coating with mixture layers and sandwich-like-structure interfaces. The proposed MDLM coating shows excellent spectral performance, and an LIDT that is almost twice of that of the TDLM coating at the two wavelengths of interest for the following reasons. First, the mixture layer in the MDLM coating has a larger optical bandgap and a lower absorption, resulting in a smaller temperature rise under the same fluence laser irradiation; second, the sandwich-like-structure interface allows the MDLM coating to exhibit enhanced mechanical properties. We believe that the described concept opens new avenues for improved dichroic mirror coatings and other laser coatings and can benefit many areas of laser technology that rely on high-quality laser coatings.

Funding. National Natural Science Foundation of China (61975215, U1831211); Youth Innovation Promotion Association of the Chinese Academy of Sciences; Strategic Priority Research Program of the Chinese Academy of Sciences (XDA25020000, XDB16030400).

Acknowledgment. The authors express their appreciation to Prof. Wolfgang Rudolph for the fruitful discussions. The authors thank Ziyuan Xu and Yun Cui for the LIDT and FIB measurements, respectively.

Disclosures. The authors declare no conflicts of interest.

REFERENCES

1. L. Ji, X. Zhao, D. Liu, Y. Gao, Y. Cui, D. Rao, W. Fang, F. Li, H. Shi, J. Liu, X. Li, L. Xia, T. Wang, J. Liu, P. Du, X. Sun, W. Ma, Z. Sui, and X. Chen, "High-efficiency second-harmonic generation of low-temporal-coherent light pulse," Opt. Lett. **44**, 4359–4362 (2019).
2. H. Jiao, X. Cheng, G. Bao, J. Han, J. Zhang, Z. Wang, M. Trubetskov, and A. V. Tikhonravov, "Study of HfO_2/SiO_2 dichroic laser mirrors with refractive index inhomogeneity," Appl. Opt. **53**, A56–A61 (2014).
3. F. Chen, J. Ma, C. Wei, R. Zhu, W. Zhou, Q. Yuan, S. Pan, J. Zhang, Y. Wen, and J. Dou, "10 kW-level spectral beam combination of two high power broad-linewidth fiber lasers by means of edge filters," Opt. Express **25**, 32783–32791 (2017).
4. M. L. Grilli, F. Menchini, A. Piegari, D. Alderighi, G. Toci, and M. Vannini, "Al_2O_3/SiO_2 and HfO_2/SiO_2 dichroic mirrors for UV solid-state lasers," Thin Solid Films **517**, 1731–1735 (2009).
5. M. L. Spaeth, P. J. Wegner, T. I. Suratwala, M. C. Nostrand, J. D. Bude, A. D. Conder, J. A. Folta, J. E. Heebner, L. M. Kegelmeyer, B. J. MacGowan, D. C. Mason, M. J. Matthews, and P. K. Whitman, "Optics recycle loop strategy for NIF operations above UV laser-induced damage threshold," Fusion Sci. Technol. **69**, 265–294 (2016).
6. A. Jeandet, A. Borot, K. Nakamura, S. W. Jolly, A. J. Gonsalves, C. Tóth, H.-S. Mao, W. P. Leemans, and F. Quéré, "Spatio-temporal structure of a petawatt femtosecond laser beam," J. Phys. Photon. **1**, 035001 (2019).
7. C. Jauregui, J. Limpert, and A. Tünnermann, "High-power fibre lasers," Nat. Photonics **7**, 861–867 (2013).
8. L. Li, X. Yang, L. Zhou, W. Xie, Y. Wang, Y. Shen, Y. Yang, W. Yang, W. Wang, Z. Lv, X. Duan, and M. Chen, "Active/passive *Q*-switching operation of 2 μm Tm, Ho:YAP laser with an acousto-optical *Q*-switch/MoS_2 saturable absorber mirror," Photon. Res. **6**, 614–619 (2018).
9. X. Liu, K. Yang, S. Zhao, T. Li, W. Qiao, H. Zhang, B. Zhang, J. Bian, L. Zheng, L. Su, and J. Xu, "High-Power passively *Q*-switched 2 μm all-solid-state laser based on a Bi_2Te_3 saturable absorber," Photon. Res. **5**, 461–466 (2017).
10. M. L. Davenport, S. Liu, and J. E. Bowers, "Integrated heterogeneous silicon/III–V mode-locked lasers," Photon. Res. **6**, 468–478 (2018).
11. S. Niu, J. Liu, F. Cheng, H. Wang, J. Zhang, N. Zhuo, S. Zhai, L. Wang, S. Liu, F. Liu, Z. Wang, X. Wang, and Z. Wei, "14 μm quantum cascade lasers based on diagonal transition and nonresonant extraction," Photon. Res. **7**, 1244–1248 (2019).
12. X. Cheng, J. Zhang, T. Ding, Z. Wei, H. Li, and Z. Wang, "The effect of an electric field on the thermomechanical damage of nodular defects in dielectric multilayer coatings irradiated by nanosecond laser pulses," Light Sci. Appl. **2**, e80 (2013).
13. J. Liu, W. Zhang, H. Cui, J. Sun, H. Li, K. Yi, and M. Zhu, "Study on high-reflective coatings of different designs at 532 nm," Chin. Opt. Lett. **12**, 083101 (2014).
14. M. Zhan, Y. Zhao, G. Tian, H. He, J. Shao, and Z. Fan, "Stress, absorptance and laser-induced damage threshold properties of 355-nm HR coatings," Appl. Phys. B **80**, 1007–1010 (2005).
15. S. Malobabic, M. Jupé, and D. Ristau, "Spatial separation effects in a guiding procedure in a modified ion-beam-sputtering process," Light Sci. Appl. **5**, e16044 (2016).
16. B. Mangote, L. Gallais, M. Commandré, M. Mende, L. Jensen, H. Ehlers, M. Jupé, D. Ristau, A. Melninkaitis, J. Mirauskas, V. Sirutkaitis, S. Kičas, T. Tolenis, and R. Drazdys, "Femtosecond laser damage resistance of oxide and mixture oxide optical coatings," Opt. Lett. **37**, 1478–1480 (2012).
17. X. Fu, A. Melnikaitis, L. Gallais, S. Kiáčas, R. Drazdys, V. Sirutkaitis, and M. Commandré, "Investigation of the distribution of laser damage precursors at 1064 nm, 12 ns on niobia-silica and zirconia-silica mixtures," Opt. Express **20**, 26089–26098 (2012).
18. M. Zhu, N. Xu, B. Roshanzadeh, S. T. P. Boyd, W. Rudolph, Y. Chai, and J. Shao, "Nanolaminate-based design for UV laser mirror coatings," Light Sci. Appl. **9**, 20 (2020).
19. K. Craig, J. Steinlechner, P. G. Murray, A. S. Bell, R. Birney, K. Haughian, J. Hough, I. Maclaren, S. Penn, S. Reid, R. Robie, S. Rowan, and I. W. Martin, "Mirror coating solution for the cryogenic Einstein telescope," Phys. Rev. Lett. **122**, 231102 (2019).
20. J. Steinlechner, I. W. Martin, A. S. Bell, J. Hough, M. Fletcher, P. G. Murray, R. Robie, S. Rowan, and R. Schnabel, "Silicon-based optical mirror coatings for ultrahigh precision metrology and sensing," Phys. Rev. Lett. **120**, 263602 (2018).
21. X. Cheng, S. Dong, S. Zhi, S. Paschel, I. Balasa, D. Ristau, and Z. Wang, "Waterproof coatings for high-power laser cavities," Light Sci. Appl. **8**, 12 (2019).
22. N. Xu, M. Zhu, Y. Chai, B. Roshanzaden, S. T. P. Boyd, W. Rudolph, Y. Zhao, R. Chen, and J. Shao, "Laser resistance dependence of interface for high-reflective coatings studied by capacitance-voltage and absorption measurement," Opt. Lett. **43**, 4538–4541 (2018).
23. H. Xing, M. Zhu, Y. Chai, K. Yi, J. Sun, Y. Cui, and J. Shao, "Improving laser damage resistance of 355 nm high-reflective coatings by co-evaporated interfaces," Opt. Lett. **41**, 1253–1256 (2016).
24. J. Tauc, R. Grigorovici, and A. Vancu, "Optical properties and electronic structure of amorphous germanium," Phys. Status Solidi **15**, 627–637 (1966).
25. H. Krol, L. Gallais, C. Grèzes-Besset, J.-Y. Natoli, and M. Commandré, "Investigation of nanoprecursors threshold distribution in laser-damage testing," Opt. Commun. **256**, 184–189 (2005).
26. Y. Xu, M. R. Abdulameer, L. A. Emmert, T. Day, D. Patel, C. S. Menoni, and W. Rudolph, "Comparison of defects responsible for nanosecond laser-induced damage and ablation in common high index optical coatings," Opt. Eng. **56**, 011019 (2017).
27. P. E. Miller, J. D. Bude, T. I. Suratwala, N. Shen, T. A. Laurence, W. A. Steele, J. Menapace, M. D. Feit, and L. L. Wong, "Fracture-Induced subbandgap absorption as a precursor to optical damage on fused silica surfaces," Opt. Lett. **35**, 2702–2704 (2010).
28. B. Bertussi, P. Cormont, S. Palmier, P. Legros, and J.-L. Rullier, "Initiation of laser-induced damage sites in fused silica optical components," Opt. Express **17**, 11469–11479 (2009).
29. L. Sun, J. Huang, H. Liu, X. Ye, J. Wu, X. Jiang, L. Yang, W. Zheng, and W. Wu, "Combination of reaction ion etching and dynamic chemical etching for improving laser damage resistance of fused silica optical surfaces," Opt. Lett. **41**, 4464–4467 (2016).
30. K. Wang, B. Ma, J. Han, H. Jiao, X. Cheng, and Z. Wang, "Morphological and damage growth characteristics of shell-type damage of fused silica optics induced by ultraviolet laser pulses," Appl. Opt. **58**, 8882–8888 (2019).
31. Q. Wu, "Extraction of extinction coefficient of weak absorbing thin films form special absorption," J. Phys. D **22**, 1384–1385 (1989).